

Near-Space Vehicle-Borne SAR With Reflector Antenna for High-Resolution and Wide-Swath Remote Sensing

Wen-Qin Wang, *Member, IEEE*

Abstract—Near-space is recognized as the atmospheric region from 20 to 100 km above the Earth's surface. Near-space vehicles offer several advantages compared to low earth orbit satellites and airplanes because near-space vehicles are not constrained by orbital mechanics and fuel consumption. These advantages provide potential for future remote sensing applications, but little related work has been published. This paper explains what near-space is and how it should be exploited for remote sensing applications. A near-space vehicle-borne synthetic aperture radar (SAR) with reflector antenna and digital beamforming on receive is proposed for high-resolution and wide-swath (HRWS) remote sensing. The system configuration, signal model, imaging scheme, system performance, and nadir echo suppression are investigated. An example system is conceptually designed, along with its system performance analysis. It is shown that the near-space vehicle-borne SAR with reflector antenna can operate with high flexibility and reconfigurability, thus enabling a satisfactory HRWS remote sensing performance.

Index Terms—Digital beamforming (DBF), high resolution and wide swath (HRWS), near-space, near-space vehicle, reflector antenna, scan-on-receive (SCORE), synthetic aperture radar (SAR).

I. INTRODUCTION

SPACE technology has greatly revolutionized modern microwave remote sensing [1]–[3]. However, the high revisiting frequency, high resolution, and robust survivability that we have desperately wanted are still difficult to be obtained for current spaceborne and airborne sensors. For example, spaceborne and airborne synthetic aperture radar (SAR) systems have received special interest in remote sensing applications [4] and have been testified by the increased number of recent and forthcoming missions, e.g., TerraSAR-X SAR [5], [6] and TanDEM-X SAR [7]. Even so, it is impossible to achieve high azimuth resolution and, simultaneously, wide swath and high

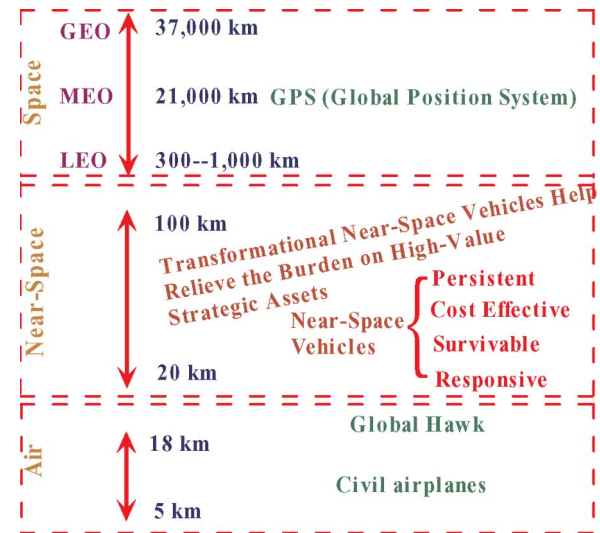


Fig. 1. Near-space definition and its advantages while compared to space, including geosynchronous orbit, middle earth orbit, LEO, and airplane.

revisiting frequency for conventional spaceborne and airborne SARs [7]. Spaceborne SAR has an imaging capability of wide swath with a limited azimuth resolution. In contrast, airborne SAR has an imaging capability of high resolution but with a limited swath coverage. There is therefore a clear incentive consideration to increase swath width and azimuth resolution simultaneously [8]. We thus have two gaps: one is the capability in high-resolution and wide-swath (HRWS) remote sensing, and the other is that there is a lack of sensors operating in the altitude between satellites and airplanes. These two gaps can be simultaneously filled by using near-space vehicles as the radar platforms [9].

Near-space is recognized as the altitudes between 20 km and 100 km [10]. It is high for airplanes and too low for satellites. However, advances have been made so that some vehicles can operate in near-space. As shown in Fig. 1, near-space vehicles offer several advantages such as persistence, robust survivability, and cost efficiency. Additionally, near-space vehicles are 10 to 20 times closer to their targets than a typical 400 km low earth orbit (LEO) satellite. This differential distance implies that near-space vehicles could detect much weaker signals. These advantages are particularly valuable for future remote sensing. Currently, there are two categories of vehicles that can fly or float in near-space [11]. Fig. 2 shows several typical near-space vehicles. The first category is free-floater, which can

Manuscript received November 29, 2010; revised April 3, 2011; accepted May 8, 2011. Date of publication June 27, 2011; date of current version January 20, 2012. This work was supported in part by the Doctoral Program of Higher Education for New Teachers under contract 200806141101, by the Fundamental Research Fund for the Central Universities under contract ZYGX2010J001, and by the open funds of the State Key Laboratory of Remote Sensing Science under contract OFSLRSS201011 and the Key Laboratory of Ocean Circulation and Waves, Chinese Academy of Sciences, under contract KLOCAW1004.

The author is with the School of Communication and Information Engineering, University of Electronic Science and Technology of China, Chengdu 610054, China (e-mail: wqwang@uestc.edu.cn).

Color versions of one or more of the figures in this paper are available online at <http://ieeexplore.ieee.org>.

Digital Object Identifier 10.1109/TGRS.2011.2158224

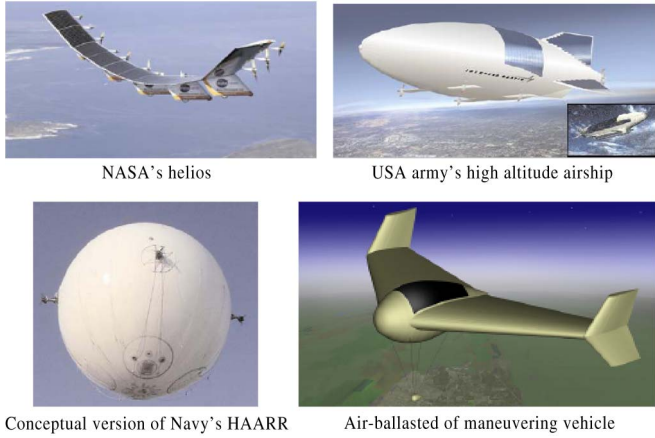


Fig. 2. Several typical near-space vehicles.

be further classified into free-floating balloon and steered free-floater. The flying speed and direction of free-floating balloons depend primarily on existing winds. Free-floating balloons can take tens to thousands of pounds to over 30 km [12]–[14]. Steered free-floaters also drift on wind, but they are able to exploit the wind to maneuver at will. Free-floaters can provide a persistent coverage which is currently impossible for satellites and airplanes by means of today's state-of-the-art technology [15].

The second category is maneuvering vehicles which can use a variety of different propulsion mechanisms to fly or keep station over an area of interest from days to months [16]. They can provide a large footprint and a long mission that are commonly associated with satellites and the responsiveness of an unmanned aerial vehicle. Not constrained by orbital mechanics like satellites, maneuvering vehicles can move at a speed as fast as 1000–1500 m/s, with a maximal payload of 4000 pounds [11]. Maneuvering vehicles are potentially the most useful type for remote sensing applications, so this paper considers only the maneuvering vehicles.

Near-space vehicles provide a new opportunity to develop new remote sensing techniques. However, little work on the use of near-space vehicle-borne sensors for communication and navigation applications has been reported [17]. Even less work on near-space vehicle-borne SAR has been reported [18], [19]. In this paper, we consider near-space vehicle-borne SAR for HRWS remote sensing. Simultaneous HRWS imaging is particularly important for remote sensing applications [20], [21], but it cannot be obtained for conventional spaceborne and airborne SARs [22]. ScanSAR allows wider swaths by employing a burst mode of data acquisition [23]. However, ScanSAR achieves a wider swath at the expense of degraded azimuth resolution or fewer imaging looks. An approach, including burst-mode operation, antenna scanning in azimuth during each burst, and elevation steering to illuminate different subswaths, was proposed in [24]. It involves the same tradeoffs between azimuth resolution and swath width.

Aiming to provide an approach for HRWS remote sensing, this paper presents the near-space vehicle-borne SAR using the reflector antenna with digital beamforming (DBF) on receive. The reflector antenna consists of a parabolic reflector and a

feed array of transmit/receive elements, which are arranged in the plane perpendicular to the flight direction and facing the reflector [25]–[30]. Each element results in a beam, illuminating a region which partially overlaps with the region illuminated by the beams of the adjacent elements. The beams can progressively scan in both azimuth and elevation. This paper focuses on the role of near-space vehicle-borne SAR with reflector antenna for HRWS remote sensing and deals with imaging scheme and performance analysis. The system concept, signal model, processing algorithm, and conceptual example are presented.

The remaining sections are organized as follows. The problem formation and motivation are discussed in Section II. The near-space vehicle-borne SAR architecture and operation are presented in Section III, followed by the performance analysis in Section IV. Next, Section V proposes a novel approach to suppress the nadir echoes. Conceptual design examples and numerical simulation results are provided in Section VI. Finally, Section VII concludes this whole paper.

II. PROBLEM FORMATION AND MOTIVATION

An efficient remote sensing technique should provide high-resolution imagery over a wide area of surveillance, but there is a contradiction between azimuth resolution and width swath. A good azimuth resolution requires a short antenna to illuminate a long synthetic aperture, which results in a wide Doppler bandwidth. This calls for a high pulse repeated frequency (PRF) to sample the Doppler spectrum. Thus, azimuth resolution and ambiguity suppression impose a lower bound on the PRF, and the higher it is, the better the achievable azimuth resolution becomes, and the smaller ambiguous signals will be. However, a high PRF means a smaller swath width. The relation between the maximum imaging swath on ground W_s and the required PRF can be expressed as

$$W_s \leq \frac{c_0}{2 \cdot \sin(\eta) \cdot \text{PRF}} \quad (1)$$

where c_0 and η denote the speed of light and the incidence angle, respectively. That is to say that a low PRF is favorable to unambiguously image a wide swath on the ground.

Substituting the expression of SAR azimuth resolution ρ_a and rearranging the terms in (1), we then have

$$\frac{W_s}{\rho_a} \leq \frac{c_0}{2 \cdot v_s \cdot \sin(\eta)} \quad (2)$$

where v_s is the SAR platform velocity. Generally, c_0/v_s is nearly constant at 20 000 for LEO spaceborne SARs and typically in the range of 300 000–750 000 for airborne SARs. Near-space vehicles can fly at a speed ranging from stationary to 1500 m/s, and the corresponding c_0/v_s will be greater than 100 000. Thus, when compared to spaceborne and airborne SARs, near-space vehicle-borne SAR provides a more flexible choice between azimuth resolution and swath width for satisfactory HRWS remote sensing.

Equation (2) can also be reformed into the basic minimum antenna area (A_{antenna}) constraint

$$A_{\text{antenna}} \geq \frac{4v_s \lambda R_c \cdot \tan(\eta)}{c_0} \quad (3)$$

where λ is the radar wavelength and R_c is the slant range from the radar to the midswath. This means that, in conventional SARs, the unambiguous swath width and the achievable azimuth resolution impose contradicting requirements on system design, and consequently, it allows only a concession between azimuth resolution and swath width. This motivated the development of several advanced imaging modes with different tradeoffs between azimuth resolution and swath width.

Several multichannel- or multiaperture-based techniques [31]–[38], such as multichannel in azimuth and multiaperture in elevation, have been proposed to alleviate the requirements imposed on the minimum antenna area. One representative approach is the displaced phase center antenna (DPCA) technique [22]. The basic idea is to divide the receive antenna in the along-track direction into multiple subapertures. In this way, the DPCA SAR benefits from the whole antenna length regarding azimuth ambiguity suppression, while azimuth resolution is determined by the length of a single subaperture, thus decoupling the restrictions on HRWS remote sensing. However, the relation between platform speed and along-track subchannel offset has to be adjusted in order to obtain a signal that is equivalently sampled as a single-channel signal of the same effective sampling rate [39]–[41]. Another potential approach is the quad-element array [31], which combines the advantages of gathering additional samples in azimuth to suppress azimuth ambiguities and simultaneously enabling an enlarged swath for a fixed PRF. However, this approach may result in a swath that is no longer continuous because the receiver must be switched off during transmission.

As DBF on receive is a promising candidate for HRWS remote sensing [42]–[45], in the following sections, we concentrate on the reflector-antenna-based DBF SAR solution. In contrast to current literatures on reflector-antenna-based spaceborne SARs [46]–[48], this paper focuses on the near-space vehicle-borne SAR imaging performance, ambiguity analysis, nadir interference suppression, and conceptual design examples, with an aim for HRWS remote sensing.

III. SYSTEM ARCHITECTURE AND IMAGING SCHEME

In SAR remote sensing missions, the antenna is a key element to total system performance. Designing one customized antenna with features like wide swath and high resolution is a technical challenge in current SAR systems. As a SAR antenna acts like a 2-D spatial filter, requirements imposed on both azimuth and elevation patterns are important. To obtain HRWS imaging for the near-space vehicle-borne SAR, a reflector antenna with multiple feed elements and a DBF technique are employed in this paper. As shown in Fig. 3, the reflector-antenna-based near-space vehicle-borne SAR involves DBF in elevation and DBF in azimuth, which are discussed, respectively, in the following two sections.

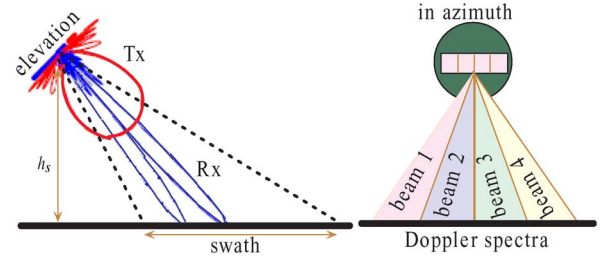


Fig. 3. Reflector-antenna-based system architecture with DBF in elevation and azimuth.

A. DBF in Elevation

To implement wide-swath imaging, the reflector-antenna-based DBF in elevation is employed in this paper. The reflector antenna consists of a parabolic reflector and a feed array of transmit/receive elements. To illuminate a given angular segment in elevation, only the corresponding feed elements are activated. On transmit, activating all elements generates a wide beam illuminating the complete swath. On receive, the reflected signals illuminate the entire reflector antenna, but they are focused on individual feed elements. The receive beam scans the complete swath within the time period of one pulse repetition interval $1/\text{PRF}$, whereas each element is only active during a subinterval of this time period. When a high PRF is employed, multiple portions of the swath will be illuminated instantaneously, but each activates a different subset of the feed elements because of different angles of arrival (DOA) [27], [46]. Equivalently, a wide swath can be obtained.

For a strictly spherical earth model, the DOA of a point target echo is associated by

$$\eta_s(t_d) = \arccos \left(\frac{(h_s + R_e)^2 + R_e^2 + R^2(t_d)}{2(h_s + R_e)R(t_d)} \right) \quad (4)$$

where h_s is the near-space vehicle's height, R_e is the Earth's radius, and $R(t_d)$, with t_d as the two-way time delay, is the slant-range distance to one given target. Thus, there is a one-to-one relation between the required beam steering angle $\eta_s(t_d)$ and the time variable t_d . This information provides a potential solution to wide-swath SAR imaging. It is well known that, to avoid range ambiguities resulting from the preceding and succeeding pulse echoes arriving at the antenna simultaneously, the slant range R should be [49]

$$\frac{c_0}{2} \left(\frac{i}{\text{PRF}} + T_p + \Delta T_{tr} \right) < R < \frac{c_0}{2} \left(\frac{i+1}{\text{PRF}} - T_p \right) \quad (5)$$

where i is an integer, T_p is the pulse duration, and ΔT_{tr} is the switching time between the transmission and the reception of a pulse.

Considering the SAR which operates with a PRF that is appropriate to the desired azimuth resolution requirement but with a wider (M times) swath than that implied by (5), we then have

$$\frac{c_0}{2} \left(\frac{i}{\text{PRF}} + T_p + \Delta T_{tr} \right) < R < \frac{c_0}{2} \left(\frac{i+M}{\text{PRF}} - T_p \right). \quad (6)$$

As the idea of a scan-on-receive (SCORE)-based DBF technique is to shape a time-varying elevation beam in reception such that it follows the echo of the pulse on the ground [32], we can divide the whole swath into M subswaths

$$\frac{c_0}{2} \left(\frac{i+m-1}{\text{PRF}} + T_p + \Delta T_{tr} \right) < R_m < \frac{c_0}{2} \left(\frac{i+m}{\text{PRF}} - T_p \right) \quad (7)$$

where $1 \leq m \leq M$. As a compromise between computation complexity and imaging performance, here M is determined by

$$M = \left\lceil \frac{2R_{\max} \cdot \text{PRF}}{c_0} \right\rceil - \left\lfloor \frac{2R_{\min} \cdot \text{PRF}}{c_0} \right\rfloor \quad (8)$$

where $\lceil \cdot \rceil$ and $\lfloor \cdot \rfloor$ denote, respectively, the maximum and minimum integers and R_{\max} and R_{\min} denote, respectively, the maximum and minimum slant ranges within the imaged swath. To avoid range ambiguity, for the conventional SAR system, the PRF should be satisfied with

$$\frac{n'}{R_{\min}/c_0 - T_p - \tau_{rp}} < \text{PRF} < \frac{n'+1}{R_{\max}/c_0 + \tau_{rp}} \quad (9)$$

where n' is a given integer and τ_{rp} is the receiver protecting window extension about the pulse duration T_p . However, by applying the SCORE operation mode, for the reflector-antenna-based SAR system, the PRF can only be satisfied with the relation

$$\frac{n'}{R_m/c_0 - T_p - \tau_{rp}} < \text{PRF} < \frac{n'+1}{R_{m+1}/c_0 + \tau_{rp}} \quad (10)$$

where R_m and R_{m+1} are the slant ranges to two adjacent subswaths, respectively. Comparing (9) and (10), we can see that, for the same operating PRF, a higher Doppler bandwidth can be sampled, allowing an improved azimuth resolution while keeping the range ambiguities constant, or alternately, the PRF can be reduced without an increase of azimuth ambiguities and degradation of the azimuth resolution while increasing the unambiguous imaging swath width.

Supposing that the looking-down angles of the first formed subaperture to each subswath are $\alpha_1(r), \alpha_2(r), \dots, \alpha_M(r)$, the relative phase delay from the first subswath to each formed subaperture can then be represented by [50]

$$0, \frac{2\pi d \sin(\alpha_1(r))}{\lambda}, \dots, \frac{2\pi(M-1)d \sin(\alpha_1(r))}{\lambda} \quad (11)$$

where d denotes the elevation distance between two subapertures. Similarly, for the second subswath, we have

$$0, \frac{2\pi d \sin(\alpha_2(r))}{\lambda}, \dots, \frac{2\pi(M-1)d \sin(\alpha_2(r))}{\lambda}. \quad (12)$$

Similar results can be obtained for the remaining subswaths. They can be formed as a matrix expressed in (13) (see equation at the bottom of the page) where

$$\alpha_m = \alpha \left(\frac{c_0}{2} \left(t + \frac{i+m-1}{\text{PRF}} \right) \right), \quad 1 \leq m \leq M \quad (14)$$

with

$$\alpha(x) = \arccos \left[\frac{x^2 + h_s^2 + 2h_s R_e}{2x(h_s + R_e)} \right] - \eta \quad (15)$$

where t represents the sampling time (fast time). As an analog-to-digital convertor is placed after each T/R-module in the feed array *a posteriori*, DBF on receive can then be formed in the direction of a wanted subswath. Equivalently, a large swath can be synthesized.

B. DBF in Azimuth

To further alleviate the requirements of HRWS imaging imposed on the minimum antenna area, DBF in azimuth is further employed in this paper. In planar-antenna-based DBF in azimuth systems, all subapertures cover the same angular segment, thus “seeing” the identical Doppler spectra. Consequently, for the same PRF, a higher (e.g., N times) Doppler bandwidth can be sampled, allowing an improved azimuth resolution while keeping the range ambiguities constant, or alternatively, the PRF can be reduced by $1/N$ while increasing the unambiguous range by a factor of N , thus extending the equivalent imaging swath. However, from the sampling theorem, we know that the sampled signal spectrum $X_s(f)$ is the sum of the unsampled signal spectrum $X_0(f)$. It repeats every f_s (in hertz), with f_s as the sampling frequency (in samples/second)

$$X_s(f) = f_s \sum_{n=-\infty}^{\infty} X_0(f - n \cdot f_s). \quad (16)$$

As the Doppler spectra are undersampled, subsequent azimuth processing must combine the total N receive channels, where each is subsampled with PRF and is aliased in frequency domain, to a single channel of $N \cdot \text{PRF}$ that is free of aliasing. Moreover, the relation between platform velocity and the

$$A_r(r) = \begin{bmatrix} \exp\left(j \frac{2\pi d \sin(\alpha_1)}{\lambda}\right) & \exp\left(j \frac{2\pi d \sin(\alpha_2)}{\lambda}\right) & \dots & \exp\left(j \frac{2\pi d \sin(\alpha_M)}{\lambda}\right) \\ \vdots & \vdots & \ddots & \vdots \\ \exp\left(j \frac{2\pi(M-1)d \sin(\alpha_1)}{\lambda}\right) & \exp\left(j \frac{2\pi(M-1)d \sin(\alpha_2)}{\lambda}\right) & \dots & \exp\left(j \frac{2\pi(M-1)d \sin(\alpha_M)}{\lambda}\right) \end{bmatrix} \quad (13)$$

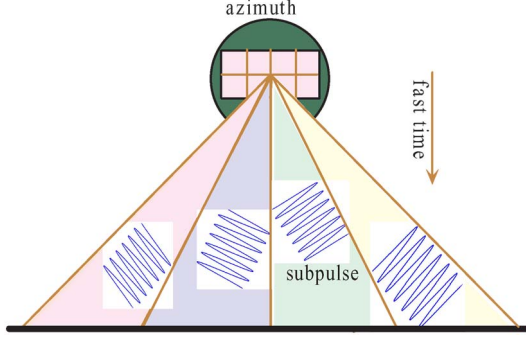


Fig. 4. Modified multidimensional waveform encoding in azimuth.

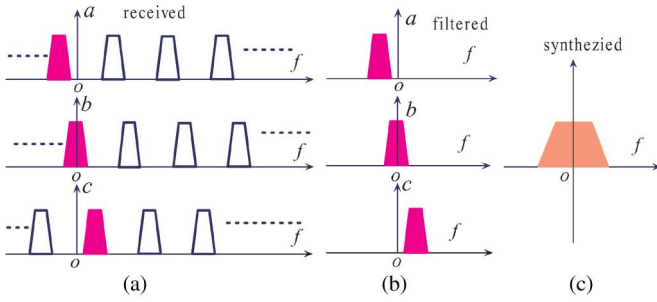


Fig. 5. Doppler spectrum synthesis in case of three azimuthal beams.

along-track offsets of the azimuth subchannels must result in equally spaced effective phase centers; otherwise, there will be nonuniform spatial sampling which makes the subsequent Doppler spectrum synthesis a challenge [51].

In contrast to conventional planar-antenna-based systems, for the reflector-antenna-based DBF in azimuth systems, there are single transmit feed and multiple receive feeds that are displaced in the along-track direction. Each azimuth element illuminates at a different angle and covers a distinct angular segment. Thus, each element samples a narrow Doppler spectrum. To exploit the large antenna array for signal transmission, the multidimensional waveform encoding investigated in [52] is modified and applied in the azimuth direction. As shown in Fig. 4, in azimuth, a series of subpulses, instead of a wide duration pulse, is transmitted, where each subpulse is separately transmitted with a different short time delay by different transmit beams.

Note that the PRF must be high enough such that the spatial sampling for each beam or channel is adequate. If the Doppler spectra of the elements are contiguous, they can jointly yield a higher azimuth resolution [53], $D/(2N)$, where D is the reflector antenna diameter. Taking three azimuth beams as an example, Fig. 5 shows the corresponding principle of Doppler spectrum synthesis.

IV. IMAGING PERFORMANCE ANALYSIS

Antenna beam shape, especially its sidelobe characteristics, is also a key to the imaging performance. Ambiguity noise

is thus an important consideration. The constraints expressed in (6) and (7) are approximate, and the required signal-to-ambiguity-noise ratio may not be met. Range ambiguities arise when the preceding and succeeding pulses may arrive back at the antenna simultaneously with the desired returns. Similarly, azimuth ambiguities arise from finite sampling of the Doppler spectrum. Since the spectrum repeats at PRF intervals, the signal components outside this frequency interval will fold back into the main part of the spectrum.

A. RASR

At a given time t within the data record window, range ambiguous signals arrive from the ranges of

$$R_j = \frac{c_0}{2} \left(\frac{m+j-1}{\text{PRF}} + t \right), \quad m = 1, 2, \dots, M; j = \pm 1, \pm 2, \dots, \pm N_h \quad (17)$$

where j , which is the pulse number ($j = 0$ for the desired pulse), is positive for the preceding pulses and negative for the succeeding ones. $j = N_h$ is the number of pulses to the horizon. We can see that this expression is different from the expression for single-aperture SAR systems, which is

$$R_j = \frac{c_0}{2} \left(\frac{j}{\text{PRF}} + t \right), \quad j = \pm 1, \pm 2, \dots, \pm N_h. \quad (18)$$

The range ambiguity is evaluated by the range-ambiguity-to-signal ratio (RASR), which is determined by summing all signal components within the data record window arising from the preceding and succeeding pulses and by taking the ratio of this sum to the integrated signal return from the desired pulse [54]

$$\text{RASR} = \frac{\sum_j \int_{R_{\min}}^{R_{\max}} \sum_1^M \frac{\gamma_{jm} G_j^2 \sigma_j}{R_j^3 \sin(\alpha_j)}}{\int_{R_{\min}}^{R_{\max}} \frac{G_0^2 \sigma_0}{R_0^3 \sin(\alpha_0)}}. \quad (19)$$

where γ_{jm} is the beamforming gain of the m th subswath at the range of R_j , G_j is the cross-track antenna pattern at the j th time interval of the data recording window at a given α_j , and σ_j is the corresponding normalized backscatter coefficient. G_0 , σ_0 , R_0 , and α_0 are the corresponding parameters of the desired unambiguous return.

B. AASR

The desired azimuth signal will also be contaminated by the ambiguous signals coming from adjacent spectra. For the

reflector-antenna-based SAR system, the azimuth-ambiguity-to-signal ratio (AASR) for the k th beam can be derived as (20) [55]

$$\begin{aligned}
 AASR_k(\text{PRF}) &= \left\{ \sum_{\substack{m=-\infty \\ m \neq 0}}^{\infty} \left[\int_{f_{dc,k}-B_d/2}^{f_{dc,k}+B_d/2} G_k^2(f + m \cdot \text{PRF}) df \right. \right. \\
 &\quad \left. \left. + \sum_{j \neq k} \int_{f_{dc,k}-B_d/2}^{f_{dc,k}+B_d/2} \Gamma_{k,j} \cdot G_k(f + m \cdot \text{PRF}) \right. \right. \\
 &\quad \left. \left. \cdot G_j(f + m \cdot \text{PRF}) df \right] \right\} \\
 &\times \left\{ \int_{f_{dc,k}-B_d/2}^{f_{dc,k}+B_d/2} G_k^2(f) df \right. \\
 &\quad \left. + \sum_{j \neq k} \int_{f_{dc,k}-B_d/2}^{f_{dc,k}+B_d/2} \Gamma_{k,j} \cdot G_k(f) \cdot G_j(f) df \right\}^{-1} \\
 &\quad (k, j) \in [1, 2, 3, \dots]
 \end{aligned} \quad (20)$$

where

$$G_{k/j}(f) = \text{sinc}^2 \left(\frac{L_a \cdot \cos(\eta_{k/j}) \cdot (f - f_{dc,k/j})}{2v_s} \right) \quad (21)$$

is the azimuth antenna pattern, L_a is the azimuth antenna length, and $\eta_{k/j}$ and $f_{dc,k/j}$ are the squint angle and Doppler frequency centroid for the k th or j th channel, respectively. As the antenna steering angle is computed using the correspondence between the signal delay and angle of arrival, any steering error will result in a SCORE loss. Thus, in (20), we employ an antenna pattern loss factor ($\Gamma_{k,j}$) [25]

$$\Gamma_{k,j} = \frac{\int_{(j-k)\tau_d - T_{ps}/2}^{(j-k)\tau_d + T_{ps}/2} \left| G_r \left(\tau - \frac{2R_c}{c_0} \right) \right|^2 d\tau}{\int_{-T_{ps}/2}^{T_{ps}/2} \left| G_r \left(\tau - \frac{2R_c}{c_0} \right) \right|^2 d\tau}, \quad k \neq j \quad (22)$$

where τ_d is the time delay between two adjoining subpulses, T_{ps} is the subpulse duration, τ is the azimuth slow time, and $G_r(\tau)$ is the receive antenna's elevation pattern.

C. NESZ

The target reflected power available at the near-space vehicle-borne receiver antenna is determined by

$$P_r = \frac{P_t \cdot G_t(\eta_i)}{4 \cdot \pi \cdot R_0^2(\eta_i)} \cdot \frac{\sigma_0}{4 \cdot \pi \cdot R_0^2(\eta_i)} \cdot \frac{\lambda^2 \cdot G_r(\eta_i)}{4 \cdot \pi} \quad (23)$$

where P_t is the transmit peak power, $G_t(\eta_i)$ and $G_r(\eta_i)$ with η_i incidence angle are the transmit and receive antenna gains, respectively, σ_0 is the radar cross section (RCS) coefficient, and $R_0(\eta_i)$ is the slant range. As the total data samples are processed coherently to produce a single imaging resolution cell,

the receiver thermal noise samples can be taken as independent from sample to sample within each pulse and from pulse to pulse. After coherent range and azimuth compression, the final image signal-to-noise ratio (SNR) can be represented by

$$\text{SNR}_{\text{image}} = \frac{P_t \cdot G_t(\eta_i) \cdot G_r(\eta_i) \cdot \lambda^3 c_0 T_p \sigma_0 \cdot \text{PRF}}{256 \pi^3 v_s \cdot R_0^3(\eta_i) \cdot \sin(\eta_i) \cdot K_0 T_{\text{sys}} B_n F_n L_s} \quad (24)$$

where T_p is the pulse duration, K_0 ($K_0 = 1.38 \times 10^{-23}$) is the Boltzmann constant, T_{sys} is the system noise temperature, F_n is the receiver noise figure, and L_s is the loss factor.

A quantity directly related to SAR imaging performance is the noise equivalent sigma zero (NESZ), defined as the target RCS for which the $\text{SNR}_{\text{image}}$ is equal to one ($\text{SNR}_{\text{image}} = 0$ dB). From (24), we can get [56]

$$\text{NESZ} = \frac{256 \pi^3 v_s \cdot R_0^3(\eta_i) \cdot \sin(\eta_i) \cdot K_0 T_{\text{sys}} B_n F_n L_s}{P_t \cdot G_t(\eta_i) \cdot G_r(\eta_i) \cdot \lambda^3 \cdot c_0 \cdot T_p \cdot \text{PRF}} \quad (25)$$

V. SUPPRESSING THE INTERFERENCES OF NADIR ECHOES

To implement effectively wide-swath imaging, the echoes reflected from the nadir points must be avoided. Otherwise, the nadir echoes will bring a catastrophic interference on the desired echoes due to their specular reflection. This constraint requires that the near-space vehicle altitude h_s and operating PRF should be satisfied with

$$\frac{c_0}{2} \left(\frac{i}{\text{PRF}} - T_p \right) < h_s < \frac{c_0}{2} \left(\frac{i}{\text{PRF}} + T_p + \Delta T \right) \quad (26)$$

where i is an integer. As this expression is a very rigorous constraint, here a novel method is presented. There will be imaging holes in the farthest and nearest swaths. Hence we have

$$\begin{cases} \frac{c_0}{2} \left(\frac{i+m-1}{\text{PRF}} + T_1 \right) < R_m \\ < \frac{c_0}{2} \left(\frac{i+m}{\text{PRF}} - T_p \right), & m = 1 \\ \frac{c_0}{2} \left(\frac{i+m-1}{\text{PRF}} + \Delta T \right) < R_m \\ < \frac{c_0}{2} \left(\frac{i+m}{\text{PRF}} \right), & 2 \leq m \leq M-1 \\ \frac{c_0}{2} \left(\frac{i+m-1}{\text{PRF}} + \Delta T \right) < R_m \\ < \frac{c_0}{2} \left(\frac{i+m}{\text{PRF}} + T_2 \right), & m = M \end{cases} \quad (27)$$

where

$$T_1 = \frac{2R_{\min}}{c_0} - \frac{i}{\text{PRF}}, \quad T_2 = \frac{2R_{\max}}{c_0} - \frac{i'}{\text{PRF}} \quad (28)$$

with

$$T_1 \geq T_p + \Delta T \quad T_2 \geq T_p \quad T_1 + T_2 < \frac{1}{\text{PRF}} \quad (29)$$

Note that i' is also an integer, but it is not equal to i .

From (27), we know the following.

- 1) When $T_p + \Delta T < t < T_1$, with t as the fast time, the first subswath has no returns.
- 2) When $T_1 < t < (1/\text{PRF}) - T_2$, all of the subswaths have returns.

- 3) When $(1/\text{PRF}) - T_2 < t < (1/\text{PRF}) - T_p$, the last subswath has no returns.

This information provides a potential solution to avoid nadir echoes. If we made the nadir echoes arrive in the receiver at $T_p + \Delta T < t < T_1$ and lie in the first subswath or arrive in the receiver at $(1/\text{PRF}) - T_2 < t < (1/\text{PRF}) - T_p$ and lie in the last subswath, the nadir echoes can then be suppressed with DBF on receive. To make the nadir echoes lie in the first subswath, the near-space vehicle's altitude should be

$$h_{s1} = \frac{c_o}{2} \left(\frac{i}{\text{PRF}} + t_d \right), \quad t_d < T_1. \quad (30)$$

The nadir echoes can then be suppressed by changing the steering matrix expressed in (13) into (31), shown at the bottom of the page with [see(15)]

$$\alpha_{d1} = \alpha [h_{s1}]. \quad (32)$$

Similarly, if we made the nadir echoes lie in the last subswath, the near-space vehicle altitude should be

$$h_{s2} = \frac{c_o}{2} \left(\frac{i'}{\text{PRF}} + t'_d \right), \quad T_2 < t'_d < \frac{1}{\text{PRF}}. \quad (33)$$

The nadir echoes can also be suppressed by changing the steering matrix expressed in (13) into (34), shown at the bottom of the page with $\alpha_{d2} = \alpha [h_{s2}]$ [see also (15)]. Certainly, the near-space vehicle altitudes expressed in (30) and (33) have a wider range than that expressed in (26). More importantly, the nadir echoes can be avoided in this way.

VI. CONCEPTUAL EXAMPLES AND SIMULATION RESULTS

To evaluate the quantitative performance of the near-space vehicle-borne SAR, we consider an example system. The SAR operates in X-band with a carrier frequency of 10 GHz. Table I gives the corresponding system parameters. Note that a far-field, flat-earth, free-space, and single polarization model is

TABLE I
NEAR-SPACE VEHICLE-BORNE SAR SYSTEM

Parameters	Values	Units
Carrier frequency	10	GHz
Platform velocity	500	m/s
Platform altitude	20	km
Reflector antenna length	1.5	m
Reflector antenna width	0.8	m
Earth radius	6370	km
Minimum slant range	40	km
Maximum slant range	100	km
Transmit peak power	1000	W
Pulse duration time	10	μ s
Pulse bandwidth	100	MHz
Range sampling frequency	150	MHz
Number of azimuth channel	3	--
Number of subswath	4	--

assumed. It is also assumed that the SAR moves at a constant velocity and operates in the stripmap mode. On transmit, activating all elements gives a wide low gain beam illuminating the complete swath. Fig. 6 shows a cut in the elevation and azimuth directions. On receive, the energy returned from a narrow portion of the ground illuminates the entire reflector, but it is focused on individual elements of the feed aperture because the SCORE technique is employed in the elevation.

It is worthwhile to compare its RASR performance to conventional single-aperture SAR. Using the system parameters listed in Table I, Fig. 7 shows the comparative RASR performance as a function of slant range. Note that equal parameters of PRF (= 4000 Hz) and subswath width are assumed in the simulations. To obtain efficient SAR imaging, the RASR should be smaller than -20 dB. It is noticed that the calculated RASR is -35 dB for the reflector antenna and SCORE technique combined case and -12 dB for general single-aperture case, respectively. These results clearly show that a significant RASR performance improvement is obtained for the reflector antenna and SCORE technique combined approach. This means that a wider swath can be obtained, however, without decreasing the

$$\begin{bmatrix} \exp\left(j \frac{1}{\lambda} 2\pi d \sin(\alpha_{d1})\right) & \exp\left(j \frac{1}{\lambda} 2\pi d \sin(\alpha_{d2})\right) & \cdots & \exp\left(j \frac{1}{\lambda} 2\pi d \sin(\alpha_{dM})\right) \\ \vdots & \vdots & \ddots & \vdots \\ \exp\left(j \frac{2\pi(M-1)d \sin(\alpha_{d1})}{\lambda}\right) & \exp\left(j \frac{2\pi(M-1)d \sin(\alpha_{d2})}{\lambda}\right) & \cdots & \exp\left(j \frac{2\pi(M-1)d \sin(\alpha_{dM})}{\lambda}\right) \end{bmatrix} \quad (31)$$

$$\begin{bmatrix} \exp\left(j \frac{1}{\lambda} 2\pi d \sin(\alpha_1)\right) & \exp\left(j \frac{1}{\lambda} 2\pi d \sin(\alpha_2)\right) & \cdots & \exp\left(j \frac{1}{\lambda} 2\pi d \sin(\alpha_{d2})\right) \\ \vdots & \vdots & \ddots & \vdots \\ \exp\left(j \frac{2\pi(M-1)d \sin(\alpha_1)}{\lambda}\right) & \exp\left(j \frac{2\pi(M-1)d \sin(\alpha_2)}{\lambda}\right) & \cdots & \exp\left(j \frac{2\pi(M-1)d \sin(\alpha_{d2})}{\lambda}\right) \end{bmatrix} \quad (34)$$

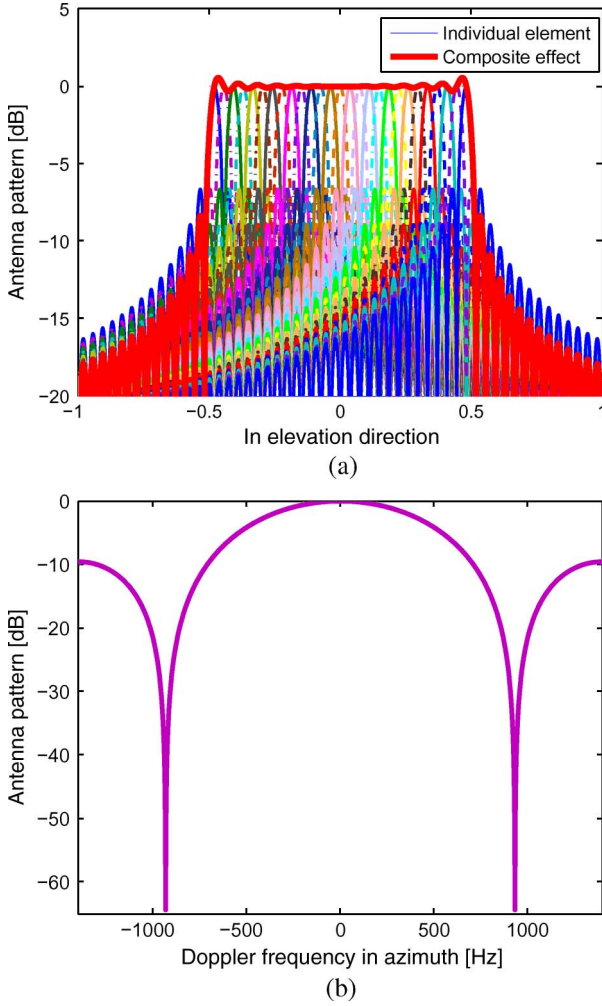


Fig. 6. Transmit antenna pattern in the elevation and azimuth directions. (a) Cut in the elevation direction. (b) Cut in the azimuth direction.

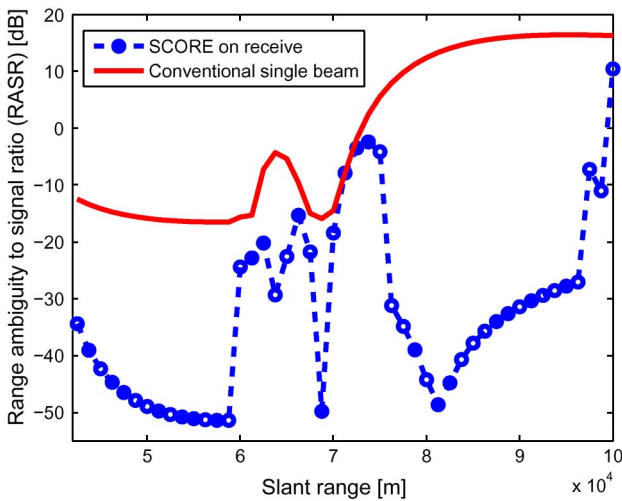


Fig. 7. Comparative RASR results between SCORE on receive and conventional single beam as a function of slant range.

operating PRF, which means that a higher azimuth resolution can be obtained.

It is also worthwhile to compare its AASR performance to conventional single-aperture SAR. Considering again the

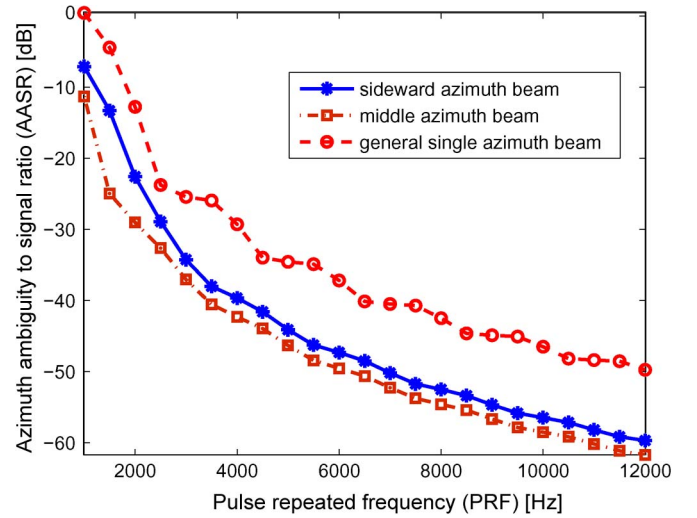


Fig. 8. Comparative AASR results of conventional single azimuth beam SAR as a function of PRF.

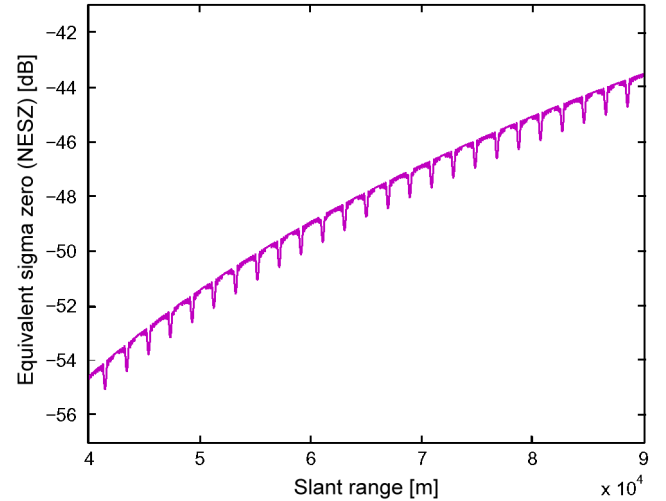


Fig. 9. NESZ results as a function of slant range.

system parameters listed in Table I, Fig. 8 shows the comparative AASR performance as a function of PRF. Note that $\Gamma_k = -10$ dB is assumed in the simulations. In SAR remote sensing applications, AASR is typically specified to be on the order of -20 dB, but a lower AASR is desired. It is shown in Fig. 8 that the AASR is typically below -20 dB, with a low operating PRF requirement. This means that a wider swath can be obtained.

Another imaging performance is the NESZ, which is shown in Fig. 9. Note that $L_s = 3$ dB and $F_n = 3$ dB are assumed in the simulation. The notches in the curve shape is caused by the switching of the active elements and the corresponding pattern switching [48]. We can notice that, for the system parameters given in Table I, the achievable swath width ranges from -54 to -44 dB. When compared to the approach investigated in [48], here the NESZ performance is improved by 20 dB. The reason is that the near-space vehicle is 10–20 times closer to the targets than the LEO satellites. This means that the near-space vehicle-borne SAR can image weaker targets, or a lower transmit power can be employed.

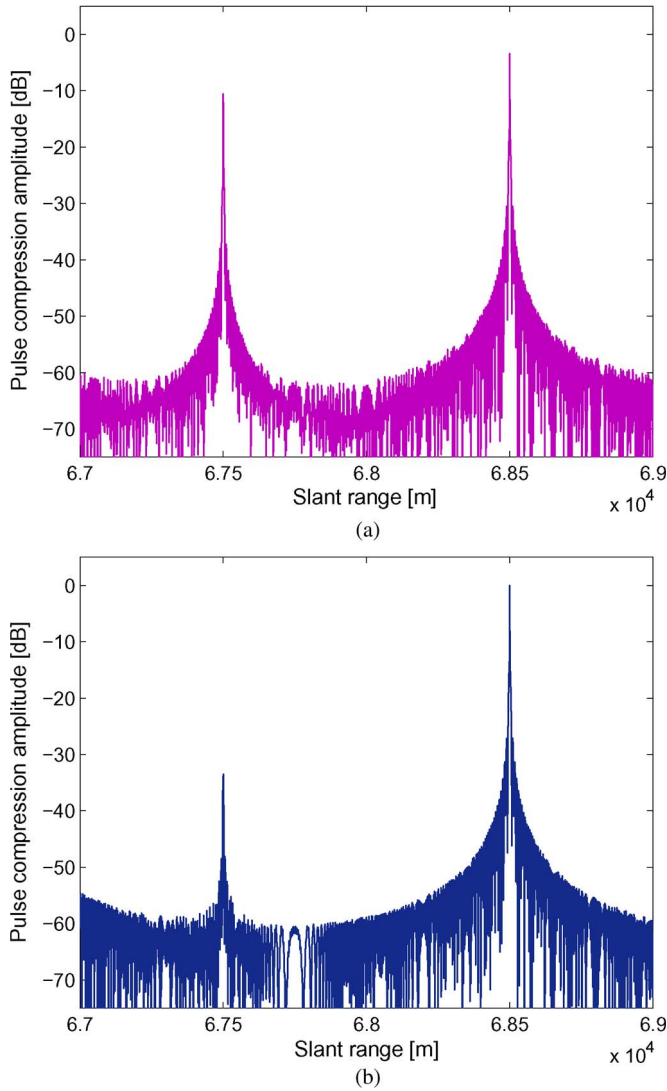


Fig. 10. Comparative pulse compression results before and after suppressing the nadir echoes. (a) Before suppressing the nadir echoes. (b) After suppressing the nadir echoes.

To analyze the performance of the nadir echo suppression approach, first, the T_1 and T_2 defined in (28) must be determined. According to the nadir echo interference suppression methods described previously, from the minimum and maximum slant ranges given in Table I, once we made the nadir echoes lie in the first or the last subswath, the nadir echoes can then be suppressed with DBF on receive. Supposing there is one point target at a slant range of 68.5 km, Fig. 10 shows the comparative pulse compression results before and after suppressing the nadir echoes. Due to range ambiguities, there is an ambiguous target located at 67.5 km in Fig. 10(a). After applying the proposed nadir echo suppression method expressed in (34), the ambiguous target is significantly suppressed, as shown in Fig. 10(b). Therefore, the nadir echoes are effectively suppressed by the proposed suppression method.

Unlike the conventional planar-antenna-based SAR system in which complex multiplication and summation are required to form a time-varying beam, digital threshold detectors are employed in the reflector-antenna-based SAR system because

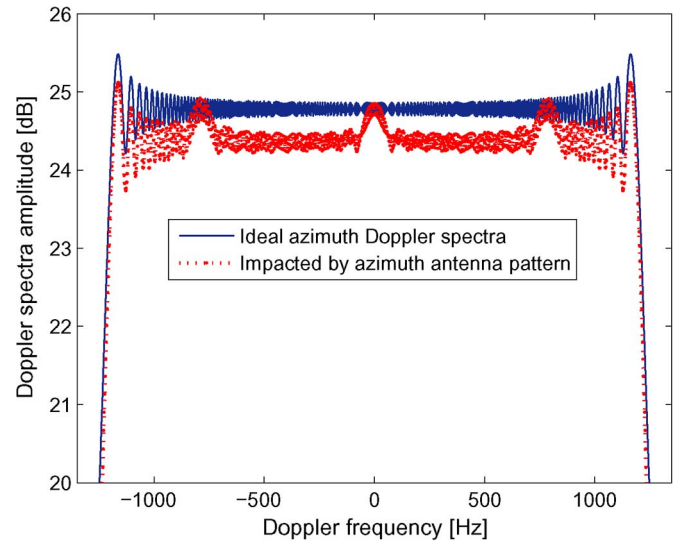


Fig. 11. Impact of azimuth antenna pattern on Doppler spectra.

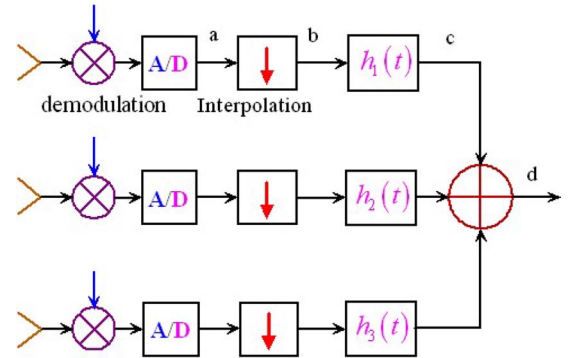


Fig. 12. Reconstruction algorithm in case of three azimuth channels.

the reflectivity variation in different scenes causes a variation of the average power level at the receiver [48]. The threshold should ensure that, at each time instance, only the information relevant channels are summed up. However, in this case, the azimuth Doppler spectrum will be undulated by the azimuth antenna pattern, as shown in Fig. 11. Consequently, the imaging performance will be degraded. This problem can be resolved by inverse filtering the azimuth multichannel signals. A block diagram for the reconstruction from the four-channel signals is shown in Fig. 12. This algorithm is based on the consideration that the azimuth signal acquisition is a linear system with multiple channels, where each can be described by a linear filter. In this case, after interpolating the data from each channel, we apply the inverse filters

$$H_k(f) = \frac{1}{\text{sinc}\left[\frac{L_a \cdot \cos(\eta_k) \cdot (f - f_{dc,k})}{2 \cdot v_s}\right]}, \quad |f - f_{dc,k}| \leq B_{as} \quad (35)$$

where B_{as} denotes the Doppler bandwidth of the azimuth channel. Note that an equal Doppler bandwidth is assumed for each azimuth channel. Finally, the inverse filtered signals can then be combined coherently. Fig. 13 shows the comparative azimuth compression results. It is noticed that improved peak-to-sidelobe and integrated sidelobe ratios can be obtained by applying the inverse filters.

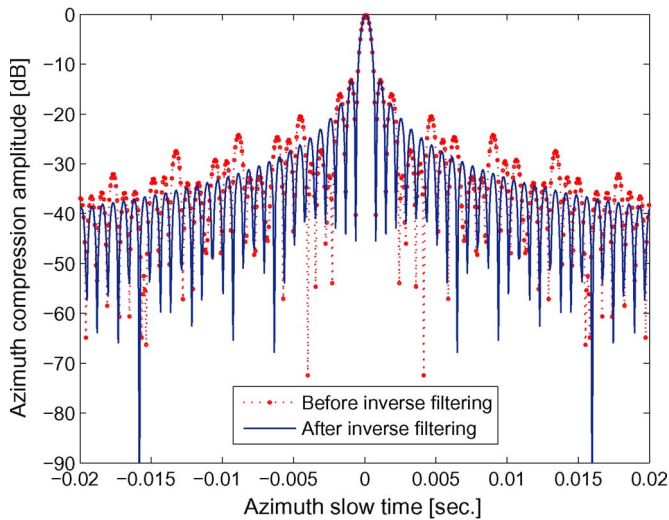


Fig. 13. Comparative azimuth compression results.

VII. CONCLUSION

Near-space vehicles provide good radar platforms for future remote sensing applications because they are more responsive and persistent than satellites and airplanes. This paper has explained what near-space is and how it could be exploited for HRWS remote sensing applications. A reflector-antenna-based near-space vehicle-borne SAR is presented for HRWS remote sensing. The imaging scheme, signal model, and system performance are investigated, along with nadir echo suppression. Comprehensive numerical simulation examples and results are provided. It is shown that the near-space vehicle-borne SAR can operate with high flexibility and reconfigurability, thus enabling satisfactory HRWS SAR remote sensing. Although near-space vehicles have a much smaller coverage area than satellites due to their lower altitude, they can still offer a regional coverage of hundreds of kilometers and can provide cost-effective remote sensing services. Near-space vehicle-borne SARs cannot replace spaceborne and airborne SARs, but they could provide more efficient remote sensing functionality than current spaceborne and airborne SARs.

One remaining problem is the required motion compensation. As a matter of fact, motion problems may arise due to the presence of atmospheric turbulence which introduces vehicle trajectory deviations from normal position, as well as altitude [57]. Motion compensation is thus required. In current spaceborne and airborne SAR systems, Global Positioning System and inertial navigation system are usually employed for this task. However, for the near-space vehicle-borne SAR, high-precision motion measurement facilities may not be reachable because of its limited load capabilities. This topic will be investigated in subsequent work.

REFERENCES

- [1] X. M. Li, S. Lehner, and T. Bruns, "Ocean wave integral parameters measurements using Envisat ASAR wave mode data," *IEEE Trans. Geosci. Remote Sens.*, vol. 49, pt. 1, no. 1, pp. 155–174, Jan. 2011.
- [2] M. Santoro, U. Wegmüller, and J. I. H. Askne, "Signatures of ERS-Envisat interferometric SAR coherence and phase of short vegetation: An analysis in the case of maize fields," *IEEE Trans. Geosci. Remote Sens.*, vol. 48, pt. 1, no. 4, pp. 1702–1713, Apr. 2010.
- [3] J. H. Gonzalez, M. Bachmann, R. Scheiber, and G. Krieger, "Definition of ICESat selection criteria for their use as height reference for TanDEM-X," *IEEE Trans. Geosci. Remote Sens.*, vol. 48, no. 6, pp. 2750–2757, Jun. 2010.
- [4] E. Trounev, G. Vasile, and M. Gay, "Combining airborne photographs and spaceborne SAR data to monitor temperate glaciers: Potentials and limits," *IEEE Trans. Geosci. Remote Sens.*, vol. 45, no. 4, pp. 905–924, Apr. 2007.
- [5] M. Eineder, C. Minet, P. Steigenberger, X. Y. Gong, and T. Fritz, "Imaging geodesy-toward centimeter-level ranging accuracy with TerraSAR-X," *IEEE Trans. Geosci. Remote Sens.*, vol. 49, no. 2, pp. 661–671, Feb. 2011.
- [6] S. Brusch, S. Lehner, T. Fritz, M. Soccorsi, A. Soloviev, and B. van Schie, "Ship surveillance with TerraSAR-X," *IEEE Trans. Geosci. Remote Sens.*, vol. 49, no. 3, pp. 1092–1103, Mar. 2011.
- [7] G. Krieger, A. Moreira, H. Fiedler, I. Hajnsek, M. Werner, M. Younis, and M. Zink, "TanDEM-X: A satellite formation for high-resolution SAR interferometry," *IEEE Trans. Geosci. Remote Sens.*, vol. 45, pt. 1, no. 11, pp. 3317–3341, Nov. 2007.
- [8] Z. F. Li, H. Y. Wang, T. Su, and Z. Bao, "Generation of wide-swath and high-resolution SAR images from multichannel small spaceborne SAR systems," *IEEE Geosci. Remote Sens. Lett.*, vol. 2, no. 1, pp. 82–86, Jan. 2005.
- [9] W. Q. Wang, "Application of near-space passive radar for homeland security," *Sens. Imag. Int. J.*, vol. 8, no. 1, pp. 39–52, Mar. 2007.
- [10] E. H. Allen, "The case for near-space," *Aerosp. Amer.*, vol. 44, no. 2, pp. 31–34, Feb. 2006.
- [11] E. B. Tomme, "Balloons in today's military: An introduction to near-space concept," *Air Space Power J.*, vol. 19, no. 4, pp. 39–50, Apr. 2005.
- [12] E. B. Tomme. (2010, Sep.). The Paradigm Shift to Effects-Based Space: Near-Space as a Combat Space Effects Enabler. [Online]. Available: <http://www.airpower.au.af.mil>
- [13] M. J. Marcel and J. Baker, "Interdisciplinary design of a near-space vehicle," in *Proc. Southeast Conf.*, Richmond, VA, Mar. 2007, pp. 421–426.
- [14] G. David and M. Mihael, *Broadband Communications via High Altitude Platforms*. Hoboken, NJ: Wiley, 2011.
- [15] W. Q. Wang, J. Y. Cai, and Q. C. Peng, "Passive ocean remote sensing by near-space vehicle-borne GPS receiver," in *Remote Sensing of The Changing Oceans*. Berlin, Germany: Springer-Verlag, 2011, ch. 5.
- [16] G. Rome and G. Frulla, "HELIPLAT: High altitude very-long endurance sonar powered UAV for telecommunication and earth observation applications," *Aeronaut. J.*, vol. 108, no. 4, pp. 2777–293, Jun. 2004.
- [17] M. Galletti, G. Krieger, B. Thomas, M. Marquart, and S. S. Johannes, "Concept design of a near-space radar for tsunami detection," in *Proc. IEEE Geosci. Remote Sens. Symp.*, Barcelona, Spain, Jul. 2007, pp. 34–37.
- [18] W. Q. Wang, J. Y. Cai, and Q. C. Peng, "Near-space SAR: A revolutionizing remote sensing mission," in *Proc. Asia-Pacific Synthetic Aperture Radar Conf.*, Huangshan, China, Nov. 2007, pp. 127–131.
- [19] W. Q. Wang, J. Y. Cai, and Q. C. Peng, "Near-space microwave radar remote sensing potentials and challenge analysis," *Remote Sens.*, vol. 2, no. 3, pp. 717–739, Mar. 2010.
- [20] M. Suess, M. Zubler, and R. Zahn, "Performance investigation on the high resolution, wide swath SAR system," in *Proc. Eur. Conf. Synthetic Aperture Radar*, Cologne, Germany, Jun. 2002, p. 187.
- [21] C. Heer, F. Soualle, R. Zahn, and R. Reber, "Investigations on a new high resolution wide swath SAR concept," in *Proc. IEEE Int. Geosci. Remote Sens. Symp.*, Toulouse, France, Jul. 2003, pp. 521–523.
- [22] A. Currie and M. A. Brown, "Wide-swath SAR," *Proc. Inst. Elect. Eng.-Radar Sonar Navig.*, vol. 139, no. 2, pp. 122–135, Apr. 1992.
- [23] R. K. Moore, J. P. Claassen, and Y. H. Lin, "Scanning spaceborne synthetic aperture radar with integrated radiometer," *IEEE Trans. Aerosp. Electron. Syst.*, vol. AES-17, no. 3, pp. 410–421, May 1981.
- [24] F. De Zan and A. M. Guarnieri, "TOPSAR: Terrain observation by progressive scans," *IEEE Trans. Geosci. Remote Sens.*, vol. 44, no. 9, pp. 2352–2360, Sep. 2006.
- [25] M. Younis, A. Patyuchenko, S. Huber, F. Bordonni, and G. Krieger, "Performance comparison of reflector- and planar-antenna based digital beam-forming SAR," *Int. J. Antenna Propag.*, vol. 2009, pp. 1–14, 2009, DOI:10.1155/2009/614931.
- [26] A. Patyuchenko, M. Younis, S. Huber, F. Bordonni, and G. Krieger, "Reflector-based digital beam-forming system for space debris detection," in *Proc. Int. Radar Symp.*, Hamburg, Germany, Sep. 2009, pp. 164–167.
- [27] M. Younis, A. Patyuchenko, S. Huber, and G. Krieger, "High performance reflector-based synthetic aperture radar—A system performance analysis," in *Proc. Int. Radar Symp.*, Vilnius, Germany, Jun. 2010, pp. 1–4.
- [28] M. Younis, A. Patyuchenko, S. Huber, G. Krieger, and A. Moreira, "A concept for a high performance reflector-based X-band SAR," in *Proc. Eur.*

- Conf. Synthetic Aperture Radar*, Aachen, Germany, Jun. 2010, pp. 740–743.
- [29] A. Damini, B. Balaji, L. Shafai, and G. Haslam, “Novel multiple phase centre reflector antenna for GMTI radar,” *Proc. Inst. Elect. Eng. Microw. Antennas Propag.*, vol. 151, no. 3, pp. 199–204, Jun. 2004.
- [30] P. Koch, C. Heer, M. Viberg, and C. G. M. Van Klooster, “Dual-polarized feed-cluster for a reflector-based multi-beam SAR antenna,” in *Proc. 17th Int. Crimean Conf. Microwave Telecommun. Technol.*, Crimea, Ukraine, Sep. 2007, pp. 815–817.
- [31] G. D. Callaghan and I. D. Longstaff, “Wide-swath spaceborne SAR using a quad-element array,” *Proc. Inst. Elect. Eng.-Radar, Sonar Navig.*, vol. 146, no. 3, pp. 159–165, Jun. 1999.
- [32] M. Suess, M. Zubler, and R. Zahn, “A novel high resolution, wide swath SAR system,” in *Proc. IEEE Int. Geosci. Remote Sens. Symp.*, Sydney, Australia, Jul. 2001, pp. 1013–1015.
- [33] C. Fischer, C. Heer, G. Krieger, and R. Werninghaus, “A high resolution wide swath SAR system,” in *Proc. Eur. Conf. Synthetic Aperture Radar*, Dresden, Germany, May 2006, pp. 1–4.
- [34] Z. F. Li, Z. Bao, H. Wang, and G. S. Liao, “Performance improvement for constellation SAR using signal processing techniques,” *IEEE Trans. Aerosp. Electron. Syst.*, vol. 42, no. 2, pp. 436–452, Apr. 2006.
- [35] Z. F. Li and Z. Bao, “A novel approach for wide-swath and high-resolution SAR image generation from distributed small spaceborne SAR systems,” *Int. J. Remote Sens.*, vol. 27, no. 5, pp. 1015–1033, Mar. 2006.
- [36] A. Jain, “Multibeam synthetic aperture radar for global oceanography,” *IEEE Trans. Antennas Propag.*, vol. AP-27, no. 4, pp. 535–538, Jul. 1979.
- [37] B. R. Jean and J. W. Rouse, “A multiple beam synthetic aperture radar design concept for geoscience applications,” *IEEE Trans. Geosci. Remote Sens.*, vol. GRS-21, no. 2, pp. 201–207, Apr. 1983.
- [38] N. Goodman, D. Rajakrishana, and J. Stiles, “Wide swath, high resolution SAR using multiple receiver apertures,” in *Proc. IEEE Int. Geosci. Remote Sens. Symp.*, Hamburg, Germany, Jun. 1999, pp. 1767–1769.
- [39] G. Krieger, N. Gebert, and A. Moreira, “Unambiguous SAR signal reconstruction from nonuniform displaced phase center sampling,” *IEEE Geosci. Remote Sens. Lett.*, vol. 1, no. 4, pp. 260–264, Oct. 2004.
- [40] P. Lombardo, F. Colone, and D. Pastina, “Monitoring and surveillance potentialities obtained by splitting the antenna of the COSMO-SkyMed SAR into multiple sub-aperture,” *Proc. Inst. Elect. Eng. Radar Sonar Navig.*, vol. 153, no. 2, pp. 104–116, Apr. 2006.
- [41] N. Gebert, G. Krieger, and A. Moreira, “Signal reconstruction from non-uniform displaced phase centre sampling in the presence of perturbations,” in *Proc. IEEE Int. Geosci. Remote Sens. Symp.*, Seoul, Korea, Jul. 2005, pp. 1034–1037.
- [42] G. Krieger and A. Moreira, “Potentials of digital beamforming in bi- and multistatic SAR,” in *Proc. IEEE Int. Geosci. Remote Sens. Symp.*, Toulouse, France, Jul. 2003, pp. 527–529.
- [43] M. Younis, C. Fischer, and W. Wiesbeck, “Digital beamforming in SAR systems,” *IEEE Trans. Geosci. Remote Sens.*, vol. 41, no. 7, pp. 1735–1739, Jul. 2003.
- [44] N. Gebert, G. Krieger, and A. Moreira, “Digital beamforming for HRWS-SAR imaging,” in *Proc. IEEE Int. Geosci. Remote Sens. Symp.*, Denver, CO, Jul. 2006, pp. 1836–1839.
- [45] N. Gebert, G. Krieger, and A. Moreira, “Digital beamforming on receive: Techniques and optimization strategies for high-resolution wide-swath SAR imaging,” *IEEE Trans. Aerosp. Electron. Syst.*, vol. 45, no. 2, pp. 564–592, Apr. 2009.
- [46] S. Huber, M. Younis, A. Patyuchenko, and G. Krieger, “Digital beam forming techniques for spaceborne reflector SAR systems,” in *Proc. Eur. Conf. Synthetic Aperture Radar*, Aachen, Germany, Jun. 2010, pp. 962–965.
- [47] A. Patyuchenko, M. Younis, S. Huber, F. Bordon, and G. Krieger, “Design aspects and performance estimation of the reflector based digital beam-forming SAR system,” in *Proc. Int. Radar Symp.*, Hamburg, Germany, Sep. 2009, pp. 1–5.
- [48] M. Younis, S. Huber, A. Patyuchenko, F. Bordon, and G. Krieger, “Digital beam-forming for spaceborne reflector- and planar-antenna SAR: A system performance comparison,” in *Proc. IEEE Int. Geosci. Remote Sens. Symp.*, Cape Town, South Africa, Jul. 2009, pp. III-733–III-736.
- [49] W. Q. Wang, Q. C. Peng, and J. Y. Cai, “Waveform-diversity-based millimeter-wave UAV remote sensing,” *IEEE Trans. Geosci. Remote Sens.*, vol. 47, no. 3, pp. 691–700, Mar. 2009.
- [50] X. Q. Wang, J. Xiao, Y. Q. Chen, and M. H. Zhu, “The SNR study of the wide-swath SAR based on elevation multi-receiver,” *J. Electron. Inf. Technol.*, vol. 29, no. 9, pp. 2101–2104, Sep. 2007.
- [51] W. Q. Wang, “Near-space wide-swath radar imaging with multiaperture antenna,” *IEEE Antennas Wireless Propag. Lett.*, vol. 8, pp. 461–464, Nov. 2009.
- [52] G. Krieger, N. Gebert, and A. Moreira, “Multidimensional waveform encoding: A new digital beamforming technique for synthetic aperture radar remote sensing,” *IEEE Trans. Geosci. Remote Sens.*, vol. 46, no. 1, pp. 31–46, Jan. 2008.
- [53] G. Krieger, N. Gebert, M. Younis, F. Bordon, A. Patyuchenko, and A. Moreira, “Advanced concepts for ultra-wide swath SAR imaging,” in *Proc. 7th Eur. Conf. Synthetic Aperture Radar*, Friedrichshafen, Germany, Jun. 2008, pp. 31–34.
- [54] J. C. Curlander and R. N. McDonough, *Synthetic Aperture Radar Systems and Signal Processing*. New York: Wiley, 1991.
- [55] F. K. Li and W. T. K. Johnson, “Ambiguities in spaceborne synthetic aperture radar systems,” *IEEE Trans. Aerosp. Electron. Syst.*, vol. AES-19, no. 3, pp. 389–397, May 1983.
- [56] G. Krieger and A. Moreira, “Spaceborne bi- and multistatic SAR: Potential and challenges,” *Proc. Inst. Elect. Eng. Radar Sonar Navig.*, vol. 153, no. 3, pp. 184–198, Jun. 2006.
- [57] Q. L. Hu and G. F. Ma, “Adaptive variable structure controller for spacecraft vibration reduction,” *IEEE Trans. Aerosp. Electron. Syst.*, vol. 44, no. 3, pp. 861–876, Jul. 2008.



Wen-Qin Wang (M'08) received the B.S. degree in electrical engineering from Shandong University, Shandong, China, in 2002 and the M.E. and Ph.D. degrees in information and communication engineering from the University of Electronic Science and Technology of China (UESTC), Chengdu, China, in 2005 and 2010, respectively.

From March 2005 to March 2007, he was with the National Key Laboratory of Microwave Imaging Technology, Chinese Academy of Sciences, Beijing, China. Since September 2007, he has been with the School of Communication and Information Engineering, UESTC, where he is currently an Assistant Professor. He is currently a Visiting Scholar at the Stevens Institute of Technology, Hoboken, NJ. His research interests include communication and radar signal processing and novel radar imaging techniques. He is the single author of one book *Multi-Antenna Synthetic Aperture Radar Imaging Theory and Practice*, in Chinese (Beijing: National Defense Industry Press, 2010), and a contributor to four books.

Dr. Wang was the recipient of the Project Investigator Innovation Award from the Wiser Foundation of Institute of Digital China in 2009. He is the Technical Program Committee Cochair of the International Conference on Computational Problem Solving, Chengdu, in 2011.